



OPEN

Facile synthesis of NiTe₂-Co₂Te₂@rGO nanocomposite for high-performance hybrid supercapacitor

Maziar Farshadnia¹, Ali A. Ensafi^{1,2}✉, Kimia Zarean Mousaabadi¹, Behzad Rezaei¹ & Muslum Demir^{3,4}

The design of bimetallic tellurides that exhibit excellent electrochemical properties remains a huge challenge for high-performance supercapacitors. In the present study, tellurium is consolidated on CoNi₂@rGO for the first time, to synthesize NiTe₂-Co₂Te₂@rGO nanocomposite by using a facile hydrothermal method. As-prepared NiTe₂-Co₂Te₂@rGO nanocomposite was characterized by EDS, TEM, FESEM, Raman, BET, XRD, and XPS techniques to prove the structural transformation. Upon the electrochemical characterization, NiTe₂-Co₂Te₂@rGO has notably presented numerous active sites and enhanced contact sites with the electrolyte solution during the faradic reaction. The as-prepared nanocomposite reveals a specific capacity of 223.6 mAh g⁻¹ in 1.0 M KOH at 1.0 A g⁻¹. Besides, it could retain 89.3% stability after 3000 consecutive galvanostatic charge–discharge cycles at 1.0 A g⁻¹ current density. The hybrid supercapacitor, fabricated by activated carbon as an anode site, and NiTe₂-Co₂Te₂@rGO as a cathode site, presents a potential window of 1.60 V with an energy density of 51 Wh kg⁻¹ and a power density of 800 W kg⁻¹; this electrode is capable of lighting up two red LED lamps and a yellow LED lamp for 20 min, which is connected in parallel. The present work opens new avenues to design and fabrication of nanocomposite electrode materials in the field of supercapacitors.

Energy storage is very important due to the significant increase in human population. Today, fossil fuels are the main energy source closely linked with global warming^{1–3}. The presence of high amounts of CO₂ in atmosphere causes heat on the earth's surface⁴. Evidence from various studies shows that atmospheric CO₂ has increased by at least 25% since the early nineteenth century. As a result, over the past 150 years, the earth's temperature has risen by more than 1 °F. To survive the earth, using renewable energy is essential to reducing greenhouse gas emissions and air pollution⁵. Therefore, new energy generation technologies like solar⁶, wind⁷, and fuel cells¹ require devices to store energy.

Batteries⁸, fuel cells⁹, and supercapacitors¹⁰ are the most important energy storage devices with high energy density and power, optimal life cycle, and mobility. Batteries and supercapacitors are two main electrical energy storage systems developed over the years for portable devices as well as smart grid deployments^{11,12}. Supercapacitors can store a large amount of charge compared to conventional capacitors, deliver energy quickly, offer fast charging ability, have a long lifetime, offer superior low-temperature performance, eco-friendly, and have low costs. Moreover, unlike batteries, they do not explode even if it is overcharged.

Electrode materials and electrolytes play an important role in achieving the best performance for commercialization of SCs^{13,14}. They affect specific capacitance, operating voltage, energy density, and power density values. Transition metal-based materials have been promising electrode materials for a long time due to their high-rate capability, high capacitance, and low cost. Still, they have limited surface area, low cycling life, and poor electrical conductivity. Hence, (1) controlling the morphology, (2) compositing the electrode materials to generate a synergic effect, (3) doping the element to electrode material to enhance redox reactivity, and (4) defect engineering are several approaches to overcome these deficiencies^{15–17}.

¹Department of Chemistry, Isfahan University of Technology, Isfahan 84156-83111, Iran. ²Department of Chemistry & Biochemistry, University of Arkansas, Fayetteville, AR 72701, USA. ³Department of Chemical Engineering, Osmaniye Korkut Ata University, Osmaniye, Turkey. ⁴Tubitak Marmara Research Center, Material Institute, Gebze 41470, Turkey. ✉email: Ensafi@iut.ac.ir; aensafi@uark.edu; aaensafi@gmail.com

Recently transition metal chalcogenides have attracted great attention as promising electrode materials for SCs applications^{18,19}. Particularly, transition metal tellurides and selenides, thanks to lower electronegativity and larger atomic radius size than sulfur and oxygen, which lead to advanced chemical, physical and electrochemical properties²⁰. The main features of these materials are long cycling life, high electrical conductivity, high mechanical stability, small ionization energy, smooth electron transport, high surface area, enhancing redox-active structures, and high specific capacitance^{21–24}. Moreover, the strong covalent bond between tellurium and cobalt/nickel increases the amounts of active sites and electrical catalytic activity. Owing to the atomic orbital overlap of tellurium with cobalt/nickel, the reduced charge-transfer band value results in enhanced supercapacitive property, flexibility, and increased charge transfer²⁵.

To date, several electrode materials for supercapacitors based on transition metal chalcogenides have been reported. For example, *Deshagani et al.*²⁶ presented the selenide doped of nickel telluride and coated it with poly(N-methylpyrrole) used for SCs application, which shows a specific capacitance of 404 C g⁻¹, the energy density of 80 Wh kg⁻¹, and power density of 400 W kg⁻¹ for asymmetric configuration signifying enhanced synergic effect of the dopant element (Se) on supercapacitor performance. *Ye et al.* fabricated the 3D hierarchical core-shell structure of NiTe@NiCoSe₂ as a positive electrode in asymmetric supercapacitors, which exhibited a maximum energy density of 59.8 Wh kg⁻¹ and power density of 800 W kg⁻¹. This device showed outstanding stability after 10,000 cycles²⁷. *Alegaonkar et al.*²⁸ presented a facile method for preparing tellurium-rGO for pseudocapacitor application and showed 168.44 F g⁻¹ at 1 A g⁻¹ in an asymmetric configuration. It has been noted that though those studies show enhanced achievement in the SC field, those materials suffer from uncontrollable experimental conditions and deficient electrode features. Herein, we applied a facile hydrothermal synthesis method to control the morphological and structural features of the as-prepared NiTe₂-Co₂Te₂@rGO nanocomposite. To the best of our knowledge, this is the first study to fabricate NiTe₂-Co₂Te₂@rGO nanocomposite with the hydrothermal method. More importantly, in-depth electrochemical characterization and practical application of SC have been implemented.

In this study, we synthesized a novel spherical NiTe₂-Co₂Te₂ grown on the reduced graphene oxide for a high-performance hybrid supercapacitor. First, CoNi₂@rGO was synthesized, then Te was introduced in this structure by ion exchange to obtain NiTe₂-Co₂Te₂@rGO, and its morphology changed. The NiTe₂-Co₂Te₂@rGO electrode reveals a specific capacity of 223.6 mAh g⁻¹ in a 1.0 M KOH at 1.0 A g⁻¹ and still retains 51.10% with the current density increasing to 10 times. Moreover, the NiTe₂-Co₂Te₂@rGO//AC, as a hybrid supercapacitor, delivers a maximal energy density of 51 Wh kg⁻¹ at 850 W kg⁻¹. The results of this study revealed that NiTe₂-Co₂Te₂@rGO nanocomposite is a promising active material as a hybrid supercapacitor with an acceptable value of energy density vs. several related materials.

Results and discussion

Structural characterization. The X-ray diffraction (XRD) pattern of NiTe₂-Co₂Te₂@rGO (12 h) in Fig. 1A reveals this nanocomposite's crystalline structure and chemical composition. The index peaks are located at 2θ = 16.2 (001), 28.2 (100)/(010), 31.6 (101)/(011), 43.15 (012), 46.75 (110), 57 (021), 62.55 (202), 77.3 (211), and 88.6 (144), corresponding to the peaks of (JCPDS card: 01-089-0504) and (JCPDS card: 96-900-8888)²⁹.

The coordinated environment of central metal ions and the valance states were investigated by X-ray photoelectron spectroscopy (XPS). Figure 1B–F proved the structure of NiTe₂-Co₂Te₂@rGO (12 h); two main peaks appeared in the high-resolution spectrum of the Ni 2p attributed to Ni 2p_{3/2} and Ni 2p_{1/2}, which indicates the

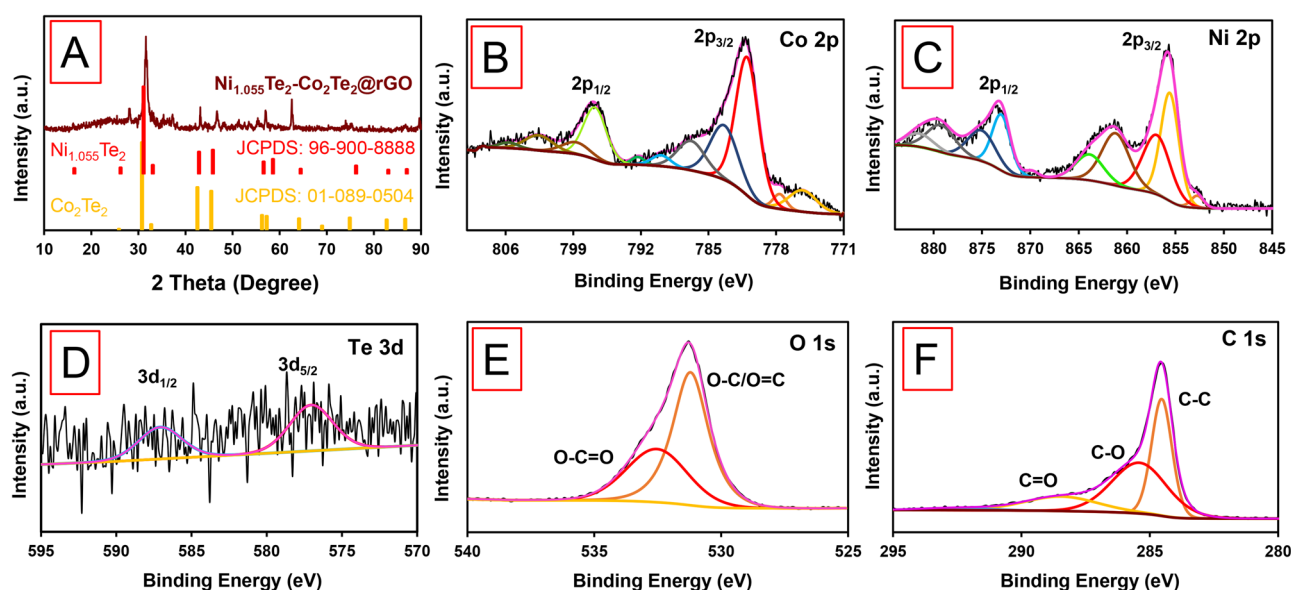


Figure 1. (A) XRD spectrum, and (B–F) High-resolution spectra of Co 2p, Ni 2p, Te 3d, O 1s, and C 1s, respectively of NiTe₂-Co₂Te₂@rGO.

existence of a mixed-valence of (Ni^{2+} and Ni^{3+}) and the Co $2p_{3/2}$ and Co $2p_{1/2}$ spectra demonstrated two main peaks contributing to Co^{2+} and Co^{3+} in the nanocomposite. Moreover, the Te $2d$ spectrum reveals two main peaks, Te $2d_{5/2}$ (577.17) and Te $2d_{3/2}$ (586.8), which are attributed to Te^{2-30} . The O $1s$ peaks at 531.8 and 532.6 eV are associated with the C=O/C–O and water/carboxylic groups, respectively. C $1s$ spectrum shows peaks at 284.5 (C–C bond), 285.6 (C–O bond), and 288.6 (C=O bond) eV in rGO. Consequently, it is detected the valence state and composition of $\text{NiTe}_2\text{-Co}_2\text{Te}_2\text{@rGO}$ to investigate the energy storage mechanism.

The morphology of $\text{NiTe}_2\text{-Co}_2\text{Te}_2\text{@rGO}$ (12 h) was investigated through microscopy images. Figure 2A–F illustrate field-emission scanning electron microscopy (FE-SEM) images of (A–B) rGO, (C–D) $\text{CoNi}_2\text{@rGO}$, and (E–F) $\text{NiTe}_2\text{-Co}_2\text{Te}_2\text{@rGO}$. GO image shows dense layers with an effective surface to enhance the rapid diffusion of the ions. CoNi_2 shows the nanowire morphology on rGO nanosheets with an average thickness of about 25 nm. The spherical $\text{NiTe}_2\text{-Co}_2\text{Te}_2\text{@rGO}$ from CoNi_2 were grown on rGO nanosheets and distributed uniformly. Moreover, this structure may provide an extensive contact area between the electrode and electrolyte because having a large specific surface area. The TEM images (Fig. 2G–H) of $\text{NiTe}_2\text{-Co}_2\text{Te}_2\text{@rGO}$ are in good agreement with the FE-SEM images. To identify the composition of the $\text{NiTe}_2\text{-Co}_2\text{Te}_2\text{@rGO}$, the EDX and elemental mapping analysis proved the existences of Ni, Co, Te, O, and C, and the distribution of elements is highly uniform (Fig. S1). Moreover, Fig. S1 exhibits that mentioned elements are uniformly distributed in the entire architecture of this composite.

The electronic structure of GO and $\text{NiTe}_2\text{-Co}_2\text{Te}_2\text{@rGO}$ materials was analyzed by Raman spectroscopy as shown in Fig. S2A. In both spectra, the band at 1555 cm^{-1} indicates the tensile vibration of the sp^2 hybrid plate, denoted G band, and represents the graphite structure. The band at 1324 cm^{-1} indicates the defect of crystal lattices of sp^3 carbon atoms, which is characterized by the D band³¹. The Raman spectra of $\text{NiTe}_2\text{-Co}_2\text{Te}_2\text{@rGO}$ displayed a blue shift in G and D-band as compared to the GO spectrum. This may be because of the enhancing number of defects in presence of Te. Another peak appeared at $\sim 980\text{ cm}^{-1}$ region in the $\text{NiTe}_2\text{-Co}_2\text{Te}_2\text{@rGO}$ due to the formation of metal hydroxide/telluride bonds that confirmed good crystallinity with strong interaction and homogeneous decoration of its particles with rGO sheets. Besides, the I_D/I_G suggests the graphitic degree of carbon materials. The I_D/I_G ratio was calculated as 0.78 and 1.0 for GO and $\text{NiTe}_2\text{-Co}_2\text{Te}_2\text{@rGO}$, respectively which indicated the generation of more in the composite.

The N_2 adsorption/desorption isotherm curve and the Barrette–Joyner–Halenda (BJH) pore size distribution of $\text{NiTe}_2\text{-Co}_2\text{Te}_2\text{@rGO}$ were illustrated in Fig. S2B. Based on the form of the hysteresis loop on the curve, it can be classified as type H3, indicating that pores are slit-like. Moreover, Based on BET and BJH data, the specific surface area, average pore size, and total pore volume are calculated as $34.49\text{ m}^2\text{ g}^{-1}$, 26.6 nm, and $0.23\text{ cm}^3\text{ g}^{-1}$, respectively. According to the results obtained from the reported analysis, it can be concluded that the $\text{NiTe}_2\text{-Co}_2\text{Te}_2\text{@rGO}$ is successfully synthesized.

Supercapacitor characterization. The electrochemical properties of $\text{CoNi}_2\text{@rGO}$, which were synthesized at different times (8, 12, and 16 h), were evaluated by CV and GCD techniques in a three-electrode setup in 1.0 M KOH. Figure S3A displays comparable CV curves of $\text{CoNi}_2\text{@rGO}$ at a scan rate of 20 mV s^{-1} . Redox peaks that appear in CV curves reveal this electrode's pseudocapacitance nature³². As illustrated, $\text{CoNi}_2\text{@rGO}$ was synthesized for 12 h, revealing a higher redox peak current density and the integrated area under the CV curve. The second synthesis step for obtained $\text{NiTe}_2\text{-Co}_2\text{Te}_2\text{@rGO}$ was performed at various times (8, 12, and 16 h). The CV curves of this structure show the same trend as $\text{CoNi}_2\text{@rGO}$, besides $\text{NiTe}_2\text{-Co}_2\text{Te}_2\text{@rGO}$ (12 h) has better reversibility in the same conditions (Fig. S3B). The corresponding GCD curves depict the same result; when synthesized for 12 h, both structures show higher specific capacity at 1 A g^{-1} current density (Fig. S3C,D). Hence, 12 h is the optimal time for both two steps of synthesis due to may be better orbital overlapping and energy band gap decrease.

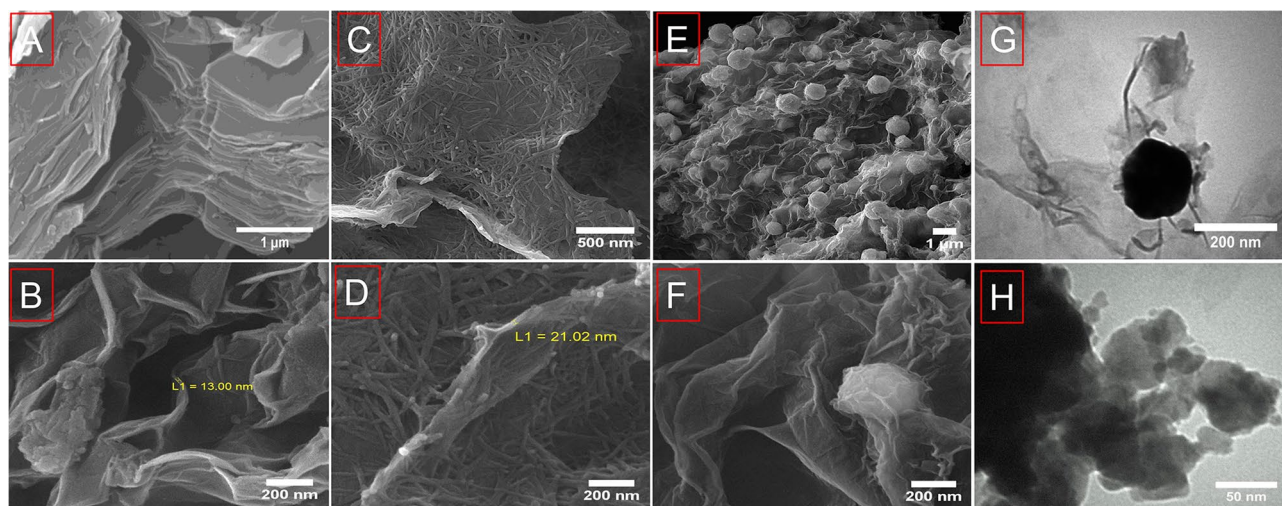


Figure 2. FE-SEM images of (A, B) GO, (C, D) $\text{CoNi}_2\text{@rGO}$ and (E–F) $\text{NiTe}_2\text{-Co}_2\text{Te}_2\text{@rGO}$; and TEM images of $\text{NiTe}_2\text{-Co}_2\text{Te}_2\text{@rGO}$ (G, H).

To investigate the synergic effect between Ni, Co, and Te in tellurides compounds, the CV curves of nickel foam (NF), $\text{CoNi}_2@\text{rGO}$, and $\text{NiTe}_2\text{-Co}_2\text{Te}_2@\text{rGO}$ are compared at a scan rate of 20 mV s^{-1} in 1.0 M KOH . The $\text{NiTe}_2\text{-Co}_2\text{Te}_2@\text{rGO}$ reveal a larger integrated area under the CV curve and a higher peak current density (Fig. 3A). Furthermore, the corresponding GCD curves are illustrated in (Fig. 3B), and The $\text{NiTe}_2\text{-Co}_2\text{Te}_2@\text{rGO}$ reveals the longest discharge time. Hereupon, tellurizing the $\text{CoNi}_2@\text{rGO}$ shows the best capacity performance due to enhancing the number of active sites and interconnection between structures and is selected for further investigation.

Figure 3C depicts CV curves of $\text{NiTe}_2\text{-Co}_2\text{Te}_2@\text{rGO}$ at different scan rates ($5\text{--}100\text{ mV s}^{-1}$) in $\text{KOH } 1.0\text{ M}$. At lower scan rates, there are two distinct anodic peaks, which are attributed to the $\text{Co}^{2+}/\text{Co}^{3+}$ and $\text{Ni}^{2+}/\text{Ni}^{3+}$ oxidation peaks, but at the higher scan rates, they merged. Moreover, the redox peak of $\text{NiTe}_2\text{-Co}_2\text{Te}_2@\text{rGO}$ is illustrated in these curves during the electrochemical process. By augmenting the scan rates, the integrated area under the CV curves tends to be bigger, but the curves' shape is not significantly changed. Thus, the reversible faradic reaction of the $\text{NiTe}_2\text{-Co}_2\text{Te}_2@\text{rGO}$ was authenticated, and the rapid ion diffusion is recommended based on previous literature as follows³⁰:

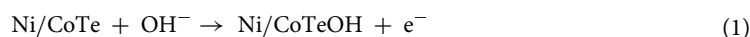


Figure 3D displays the GCD curves of $\text{NiTe}_2\text{-Co}_2\text{Te}_2@\text{rGO}$ at the different current densities ($1\text{--}10\text{ A g}^{-1}$). The specific capacity was $223.6, 196.6, 154.2, 140.0, 122.5,$ and 113.8 mAh g^{-1} at $1, 2, 5, 7, 9,$ and 10 A g^{-1} , respectively. Hence, GCD curves gradually shift left and have a quasi-symmetric shape, revealing great rate performance and coulombic efficiency. The $\text{NiTe}_2\text{-Co}_2\text{Te}_2@\text{rGO}$ can keep higher capacity retention of 51.1% than 40.3% of the $\text{CoNi}_2@\text{rGO}$, with the current density augmenting 10 times. Therefore, it diffuses ions faster than $\text{CoNi}_2@\text{rGO}$ through the electrolyte during the GCD process (Fig. 3E). Cyclic stability is the essential characteristic parameter for investigating supercapacitor performance. Figure 3F displays the 89.3% initial specific capacity of $\text{NiTe}_2\text{-Co}_2\text{Te}_2@\text{rGO}$ maintained after 3000 successive GCDs performed at a 10 A g^{-1} current density in 1.0 M KOH . The result confirms its desirable stability, but a reduction in the specific capacity resulted from the destruction of NCH/PrGO and a loss of its active sites. Table S1 depicts $\text{NiTe}_2\text{-Co}_2\text{Te}_2@\text{rGO}$ electrode presents good specific capacity than recently reported related electrode materials.

Electrochemical impedance spectroscopy (EIS) analysis was performed to study the electrode materials' resistive properties. The EIS of $\text{NiTe}_2\text{-Co}_2\text{Te}_2@\text{rGO}$ and $\text{CoNi}_2@\text{rGO}$ were tested at $100\text{ kHz--}100\text{ mHz}$ in 1.0 M KOH (Fig. 4). In the high-frequency region, the semicircle appears to be attributed to the charge transfer process, and the vertical line in the low-frequency region corresponds to the diffusion of the ions at the electrode/electrolyte interfaces. The Nyquist plot of $\text{NiTe}_2\text{-Co}_2\text{Te}_2@\text{rGO}$ illustrates a slope close to 90° revealing the fast ions

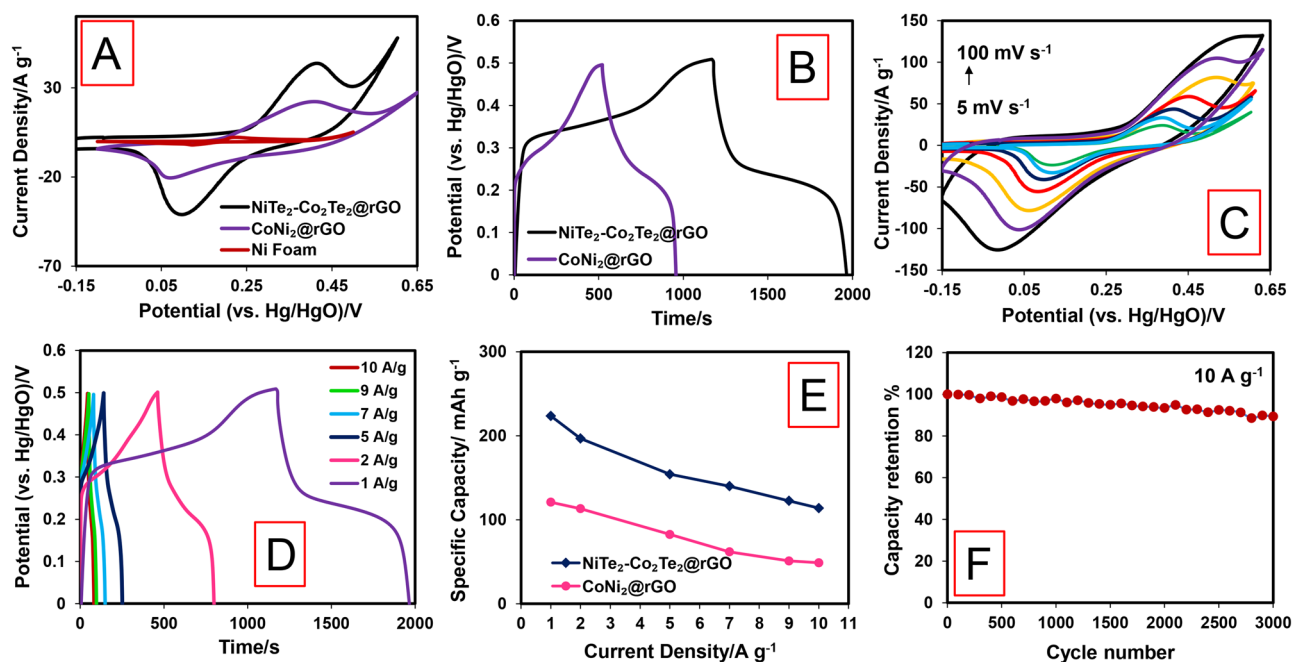


Figure 3. Electrochemical performance measurements in a three-electrode system; (A) CV curves of the NF, $\text{CoNi}_2@\text{rGO}$, and $\text{NiTe}_2\text{-Co}_2\text{Te}_2@\text{rGO}$ at a scan rate of 20 mV s^{-1} , (B) GCD curves of the $\text{CoNi}_2@\text{rGO}$ and $\text{NiTe}_2\text{-Co}_2\text{Te}_2@\text{rGO}$ electrodes at a current density of 1 A g^{-1} , (C) CV curves of $\text{NiTe}_2\text{-Co}_2\text{Te}_2@\text{rGO}$ at different scan rates of $5\text{--}100\text{ mV s}^{-1}$, (D) GCD curves of the $\text{NiTe}_2\text{-Co}_2\text{Te}_2@\text{rGO}$ electrode at various current densities, (E) The relevance of the specific capacity of the $\text{CoNi}_2@\text{rGO}$ and $\text{NiTe}_2\text{-Co}_2\text{Te}_2@\text{rGO}$ electrodes with current densities, and (F) Cycling life of $\text{NiTe}_2\text{-Co}_2\text{Te}_2@\text{rGO}$ electrode at 10.0 A g^{-1} in 1.0 M KOH .

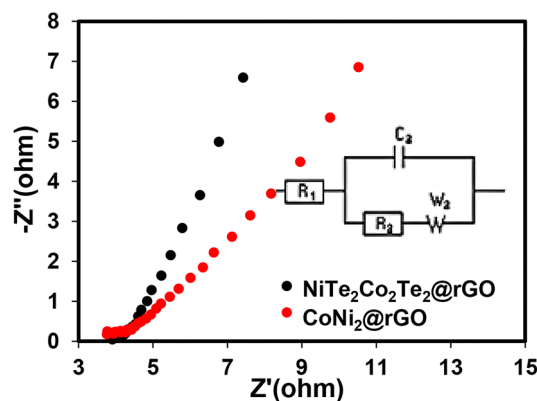


Figure 4. Nyquist plots of the CoNi₂@rGO and NiTe₂-Co₂Te₂@rGO electrodes from 100 kHz to 100 mHz at open circuit potential (Inset: equivalent circuit).

mobility between the electrode and electrolyte. The NiTe₂-Co₂Te₂@rGO curve was fitted with the Randles circuit model by Z-view software and the corresponding equivalent circuit display inset of Fig. 4. All the parameters to investigate the diffusion of the electrolytes on the electrode's surface, including W₀ (Warburg element), CPE-T (Constant phase angle exponent), CPE-T (pseudo-capacitance), R_s (Solution resistance), and R_{ct} (Charge transfer resistance) are reported in Table 1³³. W₀ can be divided into three components: W-R (Ohmic resistance), W-T (diffusion time constant), and W-P (Warburg phase exponent). Accordingly, the NiTe₂-Co₂Te₂@rGO has the lowest charge-transfer resistance due to fast ion diffusion kinetics and electronic conductivity. Moreover, it has the lowest W-R and W-T values illustrating lower shorter ion diffusion and lower Ohmic resistance. According to these electrochemical analyses, the NiTe₂-Co₂Te₂@rGO electrode displays great performance and can be used in supercapacitors.

The activated carbon was utilized as a negative electrode, and NiTe₂-Co₂Te₂@rGO as a positive electrode to fabricate a hybrid supercapacitor (HSC) device with 1.0 M KOH. Figure 5A displays the CV curves of Activated carbon and NiTe₂-Co₂Te₂@rGO in a three-electrode system to evaluate a stable working potential of negative and positive electrodes at scan rates of 20 mV s⁻¹. The working voltage of the NiTe₂-Co₂Te₂@rGO//AC HSC device was studied with CV and GCD curves at various voltage windows (Fig. 5B,C). Both CV and GCD curves reveal that the working voltage of this device is 0–1.6 V for further electrochemical measurements. The CVs were performed at different scan rates (10–90 mV s⁻¹). The shape of the CV confirmed the capacitive behavior of both electric double-layer capacity and pseudocapacitance (Fig. 5D). The GCD curves of the HSC device were performed at 1 to 10 A g⁻¹. The specific capacity was calculated as 64 mAh g⁻¹ at 1 A g⁻¹, and the retention of NiTe₂-Co₂Te₂@rGO//AC HSC device was ~63% (41 F g⁻¹) at 10 A g⁻¹ (Fig. 5E). Therefore, the high-rate capability reveals the fast kinetics properties of this device.

The stability of NiTe₂-Co₂Te₂@rGO//AC HSC device was tested by consequence GCD cycles at 10 A g⁻¹. The specific capacity of NiTe₂-Co₂Te₂@rGO//AC HSC device after 3000 GCD cycles decreases by about ~18% of its initial value. As a result of the many harsh redox reactions, the HSC device gradually lost its capacity performance after 3000 cycles (Fig. 5F). The energy density and power density were obtained from GCD curves at different current densities, and the Ragone plot is presented in Fig. 6A. The fabricated HSC device delivered a maximum 51 W h Kg⁻¹ energy density at 800 W Kg⁻¹ power density. The device also retained the energy density of 32 W h Kg⁻¹ when the power density increased to 8000 W Kg⁻¹. Besides, the energy density and power density of this device compared with other related HSCs show this device's great performance. Three assembly devices connected in series could be able to light a yellow and two red LEDs (8 mm) in parallel, and a blue LED (8 mm) for 20 and 14 min, respectively (Fig. 6B).

Methods

Synthesis of NiTe₂-Co₂Te₂@rG. Firstly, GO was synthesized by the modified hummer method³⁸. 100 mg of GO was added to 50 mL DI water and ultrasonicated for 1 h to obtain a uniform suspension (180 kW). Then, the obtained suspension was centrifuged at a speed of 2500 for 15 min, and the supernatant solution was separated. 1.6 mmol Ni(NO₃)₂·6H₂O and 0.8 mmol Co(NO₃)₂·6H₂O were added to the supernatant solution and stirred for 30 min. After that, 10 mmol urea as a reducing agent was added to the suspension, and it was

Electrode	R _s (Ω)	R _{ct} (Ω)	CPE-T (s ⁻ⁿ) × 10 ⁻⁵	CPT-P (n)	W-R (Ω)	W-P	W-T (s)
CoNi ₂ @rGO	3.76	1.92	68.5	0.91	19.2	0.65	0.042
NiTe ₂ -Co ₂ Te ₂ @rGO	3.77	0.51	9.5	0.84	4.1	0.47	0.11

Table 1. The EIS parameters of CoNi₂@rGO and NiTe₂-Co₂Te₂@rGO.

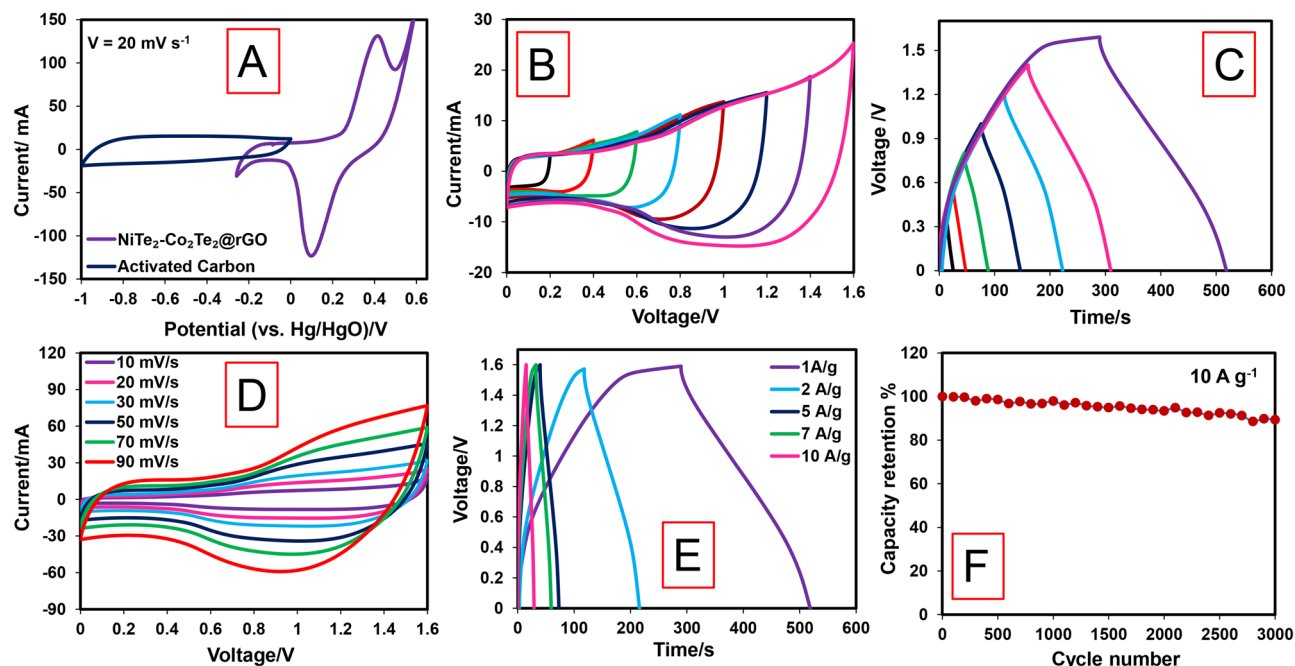


Figure 5. Electrochemical performance measurements in HSC device: (A) CV curves of the activated carbon and $\text{NiTe}_2\text{-Co}_2\text{Te}_2\text{@rGO}$ electrodes at a scan rate of 20 mV s^{-1} in a three-electrode system in 1.0 M KOH , (B) CV curves at different potential windows ($0.2\text{--}1.6 \text{ V}$) at a scan rate of 20 mV s^{-1} , (C) GCD curves at different potential windows ($0.2\text{--}1.6 \text{ V}$) at a current density of 1.0 A g^{-1} , (D) CV curves at various scan rate ($10\text{--}90 \text{ mV s}^{-1}$), (E) GCD curves at different current densities ($1\text{--}10 \text{ A g}^{-1}$), and (F) cycling performance at 10 A g^{-1} of the $\text{NiTe}_2\text{-Co}_2\text{Te}_2\text{@rGO}$ HSC device.

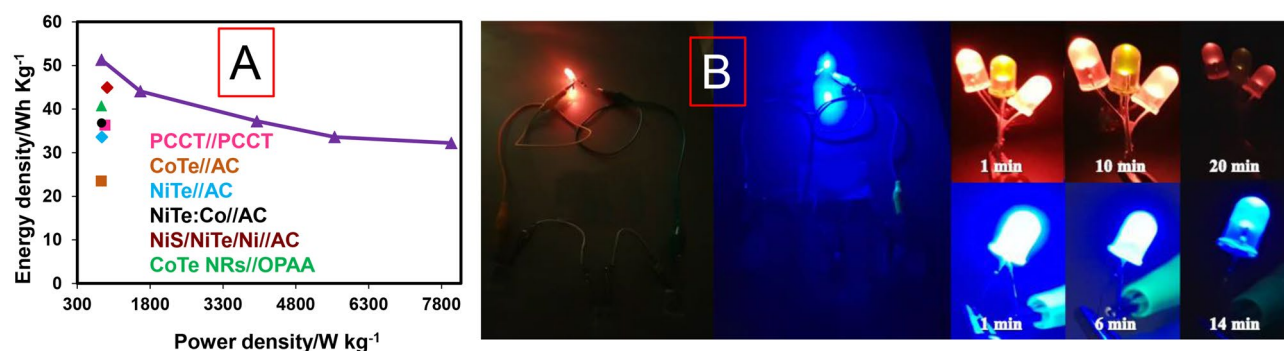


Figure 6. (A) Ragone plot of $\text{NiTe}_2\text{-Co}_2\text{Te}_2\text{@rGO//AC}$ HSC device vs. other Te-based//AC HSC devices^{18,22,34–37} and (B) The yellow and two red LEDs (8 mm) connected in parallel, and a blue LED (8 mm) turned on by three $\text{NiTe}_2\text{-Co}_2\text{Te}_2\text{@rGO//AC}$ HSC device.

stirred for 45 min and ultrasonicated for 15 min . The final suspension was transferred to the 100 ml Teflon-lined stainless-steel autoclave and kept for $8, 12,$ and 16 h at $120 \text{ }^\circ\text{C}$. Finally, the obtained product ($\text{CoNi}_2\text{@rGO}$) was freeze-drying for 24 h .

In the next step, 0.7 mmol of K_2TeO_3 was dissolved in 60 mL DI water, and 10 mL hydrazine monohydrate as a reducing agent was added, then it was stirred for 6 h . Afterward, 80 mg of $\text{CoNi}_2\text{@rGO}$ was added to the obtained solution and stirred for 1 h . This suspension was transferred to the 100 mL Teflon-lined stainless-steel autoclave and kept for $8, 12,$ and 16 h at $120 \text{ }^\circ\text{C}$. The obtained $\text{Ni}_{1.055}\text{Te}_2\text{-Co}_2\text{Te}_2\text{@rGO}$ was dried in a vacuum dryer for 6 h at $60 \text{ }^\circ\text{C}$ (Fig. 7).

Apparatus, electrochemical measurements, assembling and electrochemical measurements of the hybrid supercapacitors (HSCs) are presented in the Supplementary Information.

Conclusion

This paper presented the successful approach to synthesize spherical $\text{NiTe}_2\text{-Co}_2\text{Te}_2$ growing on rGO from CoNi_2 via two-step hydrothermal methods by anion exchange method. The optimum structure of this material for supercapacitor application was chosen by synthesizing both $\text{NiTe}_2\text{-Co}_2\text{Te}_2\text{@rGO}$ and $\text{CoNi}_2\text{@rGO}$ at different times ($6, 12,$ and 18 h), and 12 h is selected as a reaction time. Various characterization methods, such as XRD, XPS,

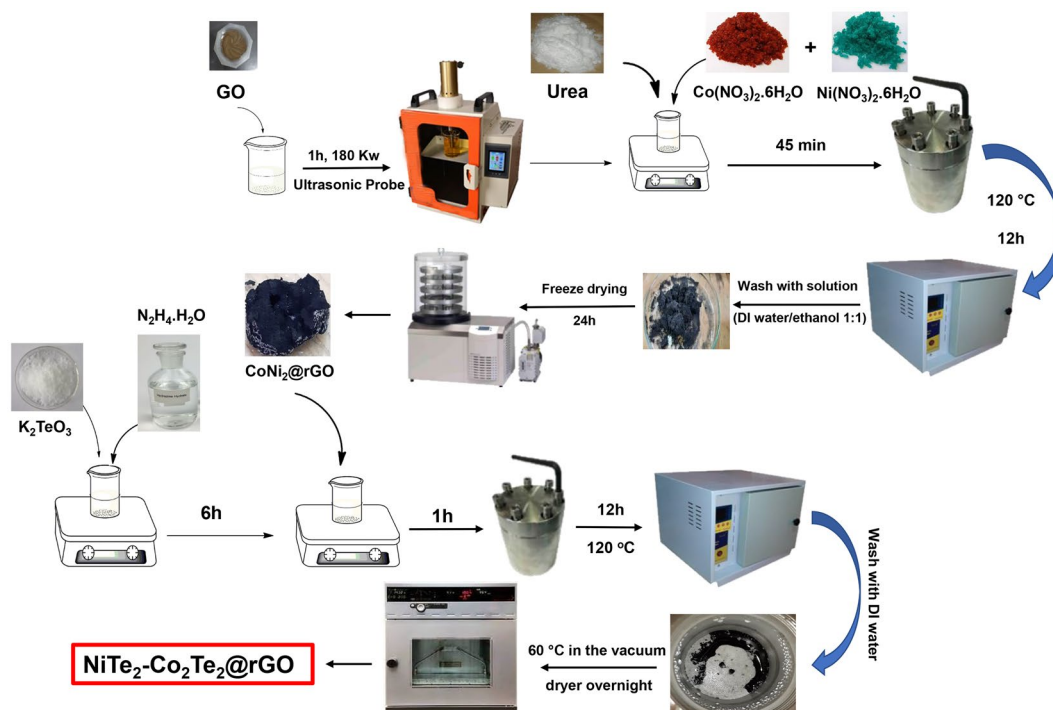


Figure 7. The synthesis procedure of NiTe₂-Co₂Te₂@rGO.

FE-SEM, EDS, elemental mapping, and TEM were used to reveal the physiochemical properties of NiTe₂-Co₂Te₂@rGO. Moreover, the electrochemical behavior of this electrode was analyzed by CV, GCD, and EIS, illustrating that this structure exposes abundant active sites, and redox reactions can be accelerated, further improving the energy storage effect as well as enhancing the efficiency of energy storage. Besides, the hybrid supercapacitor was assembled on NiTe₂-Co₂Te₂@rGO (as the positive electrode) and AC (as the negative electrode), resulting in a specific capacity of 64 mAh g⁻¹ with a high energy density of 51 Wh kg⁻¹ and power density of 800 W kg⁻¹. The excellent electrochemical performance confirms NiTe₂-Co₂Te₂@rGO's potential as an active material for HSCs for future energy storage systems in electronic devices and vehicles. Finally, this work aims to show transition metals telluride's perspective for application in energy storage systems.

Data availability

The datasets supporting the conclusions of this article are included within the article.

Received: 15 November 2022; Accepted: 20 January 2023

Published online: 24 January 2023

References

1. Olabi, A. G. & Abdelkareem, M. A. Renewable energy and climate change. *Renew. Sustain. Energy Rev.* **158**, 112111 (2022).
2. Dunlop, I. The role of the fossil fuel industry. in *Sustainability and the New Economics* 137–160 (Springer, 2022).
3. Soam, A., Mahender, C., Kumar, R. & Singh, M. Power performance of BFO-graphene composite electrodes based supercapacitor. *Mater. Res. Express* **6**, 25054 (2018).
4. Kasting, J. F. & Ackerman, T. P. Climatic consequences of very high carbon dioxide levels in the Earth's early atmosphere. *Science* **234**, 1383–1385 (1986).
5. Dincer, I. Renewable energy and sustainable development: A crucial review. *Renew. Sustain. Energy Rev.* **4**, 157–175 (2000).
6. Shahsavari, A. & Akbari, M. Potential of solar energy in developing countries for reducing energy-related emissions. *Renew. Sustain. Energy Rev.* **90**, 275–291 (2018).
7. Gu, C. & Li, H. Review on deep learning research and applications in wind and wave energy. *Energies* **15**, 1510 (2022).
8. Zhang, C., Wei, Y.-L., Cao, P.-F. & Lin, M.-C. Energy storage system: Current studies on batteries and power condition system. *Renew. Sustain. Energy Rev.* **82**, 3091–3106 (2018).
9. Smith, W. The role of fuel cells in energy storage. *J. Power Sources* **86**, 74–83 (2000).
10. Mensah-Darkwa, K., Zequine, C., Kahol, P. K. & Gupta, R. K. Supercapacitor energy storage device using biowastes: A sustainable approach to green energy. *Sustainability* **11**, 414 (2019).
11. Soam, A. Application of ferrites as electrodes for supercapacitor. *Ferrites Synth. Appl.* **55**, 99381 (2021).
12. Wang, L. *et al.* Metal-organic frameworks for energy storage: Batteries and supercapacitors. *Coord. Chem. Rev.* **307**, 361–381 (2016).
13. Zhi, M., Xiang, C., Li, J., Li, M. & Wu, N. Nanostructured carbon-metal oxide composite electrodes for supercapacitors: A review. *Nanoscale* **5**, 72–88 (2013).
14. Wang, Y. *et al.* Recent progress in carbon-based materials for supercapacitor electrodes: A review. *J. Mater. Sci.* **56**, 173–200 (2021).
15. Liu, R. *et al.* Fundamentals, advances and challenges of transition metal compounds-based supercapacitors. *Chem. Eng. J.* **412**, 128611 (2021).

16. Cherusseri, J., Choudhary, N., Kumar, K. S., Jung, Y. & Thomas, J. Recent trends in transition metal dichalcogenide based supercapacitor electrodes. *Nanosc. Horizons* **4**, 840–858 (2019).
17. Wang, T., Chen, H. C., Yu, F., Zhao, X. S. & Wang, H. Boosting the cycling stability of transition metal compounds-based supercapacitors. *Energy Storage Mater.* **16**, 545–573 (2019).
18. Zhou, P. *et al.* Facile hydrothermal synthesis of NiTe and its application as positive electrode material for asymmetric supercapacitor. *J. Alloys Compd.* **685**, 384–390 (2016).
19. Shaikh, N. S. *et al.* Novel electrodes for supercapacitor: Conducting polymers, metal oxides, chalcogenides, carbides, nitrides, MXenes, and their composites with graphene. *J. Alloys Compd.* **893**, 161998 (2022).
20. Wang, K. *et al.* Designing 3d dual transition metal electrocatalysts for oxygen evolution reaction in alkaline electrolyte: Beyond oxides. *Nano Energy* **77**, 105162 (2020).
21. Zhang, T. *et al.* One-step microwave synthesis of in situ grown NiTe nanosheets for solid-state asymmetric supercapacitors and oxygen evolution reaction. *J. Alloys Compd.* **909**, 164786 (2022).
22. Ye, B., Huang, M., Fan, L., Lin, J. & Wu, J. Co ions doped NiTe electrode material for asymmetric supercapacitor application. *J. Alloys Compd.* **776**, 993–1001 (2019).
23. Manikandan, M., Subramani, K., Sathish, M. & Dhanuskodi, S. NiTe nanorods as electrode material for high performance supercapacitor applications. *ChemistrySelect* **3**, 9034–9040 (2018).
24. Ye, B. *et al.* Construction of NiTe/NiSe composites on Ni foam for high-performance asymmetric supercapacitor. *ChemElectroChem* **5**, 507–514 (2018).
25. Qian, G. *et al.* Free-standing bimetallic CoNiTe₂ nanosheets as efficient catalysts with high stability at large current density for oxygen evolution reaction. *Renew. Energy* **162**, 2190–2196 (2020).
26. Deshagani, S., Ghosal, P. & Deepa, M. Altered crystal structure of nickel telluride by selenide doping and a poly (N-methylpyrrole) coating amplify supercapacitor performance. *Electrochim. Acta* **345**, 136200 (2020).
27. Ye, B. *et al.* Interface engineering for enhancing performance of additive-free NiTe@ NiCoSe₂ core/shell nanostructure for asymmetric supercapacitors. *J. Power Sources* **506**, 230056 (2021).
28. Alegaonkar, A. P., Mahadalkar, M. A., Alegaonkar, P. S., Kale, B. B. & Pardeshi, S. K. High performance tellurium-reduced graphene oxide pseudocapacitor electrodes. *Electrochim. Acta* **291**, 225–233 (2018).
29. Zhang, S. *et al.* Synthesis of novel bimetallic nickel cobalt telluride nanotubes on nickel foam for high-performance hybrid supercapacitors. *Inorg. Chem. Front.* **7**, 477–486 (2020).
30. Shi, C. *et al.* Granular nanosheets made of interconnected NiTe₂-CoTe₂ nanoparticles on carbon fibers for high-performance hybrid supercapacitors. *ACS Appl. Energy Mater.* **5**, 2817–2825 (2022).
31. Lakra, R. *et al.* Facile synthesis of cobalt oxide and graphene nanosheets nanocomposite for aqueous supercapacitor application. *Carbon Trends* **7**, 100144 (2022).
32. Zarean Mousaabadi, K., Ensafi, A. A. & Rezaei, B. Co₃O₄/MoCo/layered double hydroxide nanosheets for asymmetric supercapacitor. *ACS Appl. Nano Mater.* **5**(6), 8097–8104 (2022).
33. Yüksel, H., Özbay, A., Kahraman, M. & Solmaz, R. The effect of 3D silver nanodome size on hydrogen evolution activity in alkaline solution. *Int. J. Hydrogen Energy* **43**, 10586–10594 (2018).
34. Wu, X., Zhang, H., Zhai, Z.-B., Xu, J. & Huang, K.-J. Tellurium-impregnated P-doped porous carbon nanosheets as both cathode and anode for an ultrastable hybrid aqueous energy storage. *J. Mater. Chem. A* **8**, 17185–17192 (2020).
35. Ye, B. *et al.* Improved performance of a CoTe//AC asymmetric supercapacitor using a redox additive aqueous electrolyte. *RSC Adv.* **8**, 7997–8006 (2018).
36. Chen, S. *et al.* An asymmetric supercapacitor using sandwich-like NiS/NiTe/Ni positive electrode exhibits a super-long cycle life exceeding 200 000 cycles. *J. Power Sources* **438**, 227000 (2019).
37. Manikandan, M., Subramani, K., Sathish, M. & Dhanuskodi, S. Hydrothermal synthesis of cobalt telluride nanorods for a high performance hybrid asymmetric supercapacitor. *RSC Adv.* **10**, 13632–13641 (2020).
38. Ghiaci, M., Farahmand, S., Masoomi, K., Safaiee, M. & Razavizadeh, J. S. Graphene vanadic acid (GVA) as a novel heterogeneous catalyst for highly selective benzene hydroxylation under mild conditions. *Adv. Powder Technol.* **32**, 660–669 (2021).

Author contributions

M.F.: Conceptualization, Methodology, and Investigation. A.A.E.: Supervision, Conceptualization, Data curation, Validation, Writing-review, and editing. K.Z.M.: Conceptualization and Writing-original draft. B.R.: Advisor and Validation. M.D.: Conducted and analyzed the XPS data, review, and editing.

Competing interests

The authors declare no competing interests.

Additional information

Supplementary Information The online version contains supplementary material available at <https://doi.org/10.1038/s41598-023-28581-5>.

Correspondence and requests for materials should be addressed to A.A.E.

Reprints and permissions information is available at www.nature.com/reprints.

Publisher's note Springer Nature remains neutral with regard to jurisdictional claims in published maps and institutional affiliations.



Open Access This article is licensed under a Creative Commons Attribution 4.0 International License, which permits use, sharing, adaptation, distribution and reproduction in any medium or format, as long as you give appropriate credit to the original author(s) and the source, provide a link to the Creative Commons licence, and indicate if changes were made. The images or other third party material in this article are included in the article's Creative Commons licence, unless indicated otherwise in a credit line to the material. If material is not included in the article's Creative Commons licence and your intended use is not permitted by statutory regulation or exceeds the permitted use, you will need to obtain permission directly from the copyright holder. To view a copy of this licence, visit <http://creativecommons.org/licenses/by/4.0/>.

© The Author(s) 2023